Eur. Phys. J. E **8**, 465–476 (2002)
DOI 10.1140/epje/i2001-10110-y

THE EUROPEAN PHYSICAL JOURNAL E

Long-time behavior of sand ripples induced by water shear flow

A. Betat[1], C.A. Kruelle[1,a], V. Frette[1,2], and I. Rehberg[1]

[1] Experimentalphysik V, Universität Bayreuth, D-95440 Bayreuth, Germany
[2] Department of Engineering, Stord/Haugesund College, Bjørnsonsgt. 45, N-5528 Haugesund, Norway

Received 9 March 2001 and Received in final form 2 July 2002 /
Published online: 8 October 2002 –

Abstract. The formation of sand ripples under water shear flow in a narrow annular channel and the approach of the ripple pattern towards a steady state were studied experimentally. Four results are obtained: i) The mean amplitude, the average drift velocity and the mean sediment transport rate of the evolving bed shape are strongly related. A quantitative characterization of this relation is given. ii) The ripple pattern reaches a stationary state with a finite ripple amplitude and wavelength. The time needed to reach the state depends on the shear stress and may be several days. iii) The onset of ripple formation is determined by the bed shear stress, but it seems neither to depend on the grain diameter nor on the depth of the water layer. iv) The ripple amplitude, drift velocity and sediment transport in this stationary state depend on the grain size. This dependency is neither captured by the particle Reynolds number nor by the Shields parameter: an empirical scaling law is presented instead.

PACS. 45.70.-n Granular systems – 92.10.Wa Sediment transport – 92.40.Gc Erosion and sedimentation

1 Introduction

Nature is rich in striking spatial patterns: from the spotted coat of a dalmatian to the ice crystals on a windscreen, from coral reefs to meandering rivers. On sand surfaces exposed to flowing air or water, patterns of ripples are often observed; in deserts or mudflats, on riverbeds, or on the beach. These ripples are generated through the fluid motion at the upper sand layers, which shifts grains along the surface. One expects the grain-level mechanisms driving the dynamics to be different for submarine and aeolian (wind-driven) ripples [1]. In nature, there are two mechanisms driving ripples: either the oscillatory shear occurring below the surface of a water wave, or the unidirectional shear caused by wind in a desert or by water in a river. We concentrate on the latter class in this paper.

The onset of unidirectional shear-induced ripple formation has been studied in laboratory experiments: ripples are created when a water shear flow of sufficient strength is applied along a flat sand surface. The nucleation may be due to local inhomogeneities in the sediment density or size, randomly occurring turbulent fluid action, or inevitable deviations from a perfectly smooth sand surface [2,3]. The growth rates of evolving ripples have been measured more recently [4].

The mechanism for ripple formation might depend on the Reynolds number of the water flow, thus one may expect that different types of theories apply for the different parameter regimes, as discussed in references [5,6]. Under continuum descriptions, sandbed formation driven by water shear flow has been successfully treated in terms of linear stability theory [7–9]. However, the attempt to treat the formation of sand bedforms as a Kelvin-Helmholtz type of instability [10] was not successful. Recently, the instability of a particle bed sheared by a *viscous* fluid has been investigated [11] utilizing the viscous resuspension theory by Leighton and Acrivos [12] to calculate the particle transport rate.

In a different type of approach, one models explicitly the grain-level events, because the formation and motion of ripples or dunes is caused by persistent erosion and alluvium of grains. These transport processes can be modelled by cellular automata that reproduce many of the qualitative features of ripple dynamics [13–15]. The physical basis for randomly occurring particle shifts could be turbulent bursts [16].

In this paper, we present experimental observations of the ripple formation: its onset is determined by the bed shear stress, but it seems neither to depend on the grain diameter nor on the depth of the water layer.

Another issue is the existence and the properties of a final stationary state of the ripple evolution. Brush [17] and later other experimental works [18,19] reported that after adjustment of height and wavelength to the constraints set by geometry and flow pattern, mature ripples in water have a typical height of less than 3 cm with a typical

[a] e-mail: christof.kruelle@uni-bayreuth.de

length of less than 30 cm and are drifting slowly in the downstream direction.

On the other hand, some theories support the idea that ripples grow continuously in amplitude and wavelength, logarithmically in time, *i.e.*, they never reach a stationary state [15]. We find that the ripple pattern, under our experimental conditions, reaches a stationary state with a finite ripple amplitude and wavelength, although the time needed to reach that state depends on the shear stress and may be several days.

The drifting ripples can be modelled by a continuum approach invoking conservation of mass in a two-dimensional geometry. Such a calculation was introduced in reference [20] and later generalized in references [21,22] for less restrictive geometrical assumptions. They found that for a ripple of height H travelling with velocity $\tilde{v}_\mathrm{t}$ the sediment transport rate $\tilde{Q}_\mathrm{b}$ should be given by $\tilde{Q}_\mathrm{b} = H \cdot \tilde{v}_\mathrm{t}$. A comparison with the theory mentioned above was not carried out so far. We describe here a detailed experimental check of this relationship. It turns out that the relation between the amplitude, the average drift velocity and the sediment transport rate of the bed shape is valid both locally and when averaged over the whole channel, after a transient of about one day. During this transient the balance does not hold.

In continuum theories (in contrast to cellular automaton models) the grain diameter is taken into consideration only indirectly *via* the roughness of the sand surface, or is simply ignored. However, experimentally there is a clear influence of the grain size on sedimentary bedforms (see, *e.g.*, Refs. [23–27]). The results reported in the literature so far do not add up to a coherent picture of how sand ripples are influenced when the grain size is changed.

We find that the time needed to reach the stationary state varies significantly both with distance from the threshold and with grain size. We measure the dependency of the ripple amplitude, drift velocity and sediment transport on the grain size. It is neither captured by the particle Reynolds number nor by the Shields parameter: an empirical scaling law is presented instead.

As suggested by the discussion above, ripple dynamics involves a subtle interplay of many factors. Our experimental setup, which will be described in the next section, has been designed in such a way that some of these factors are well controlled. For ripple dynamics in nature, on the other hand, boundary conditions are less strict and all factors that are involved may vary considerably. As a result, ripple shapes and dynamics as observed in our experiment may differ significantly from those encountered in nature.

2 Experimental setup

Most of the previous experiments were performed in rectangular, tiltable channels. It is then necessary to continuously feed the system with water and sediment, which gives rise to uncontrolled perturbations especially near the inlet and the outlet. Examples of such setups are described in references [25,28]. Our experimental arrangement has several advantages compared to previous work: rotational symmetry, strict mass conservation, quasi–one-dimensional geometry, as well as high spatial and temporal resolution. Using this setup we have been able to measure the evolution of the amplitude, the drift velocity and the sediment transport of the ripple pattern from the early stages up to the stationary state for four different grain sizes.

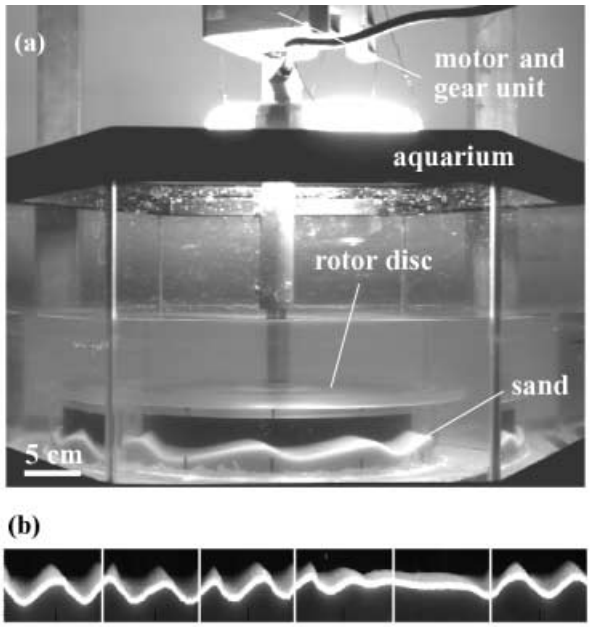

Fig. 1. (a) Side view of the experimental setup; (b) the six images of the sand-water interface are separated by vertical white lines. The images have been expanded in the vertical direction.

Table 1. Experimental conditions and critical fluid velocity $u_{\tau,\mathrm{cr}}$ for each of the sand charges. Here, d is the mean grain diameter, α the angle of repose, and h_w the depth of the water layer.

Diameter range	d	α	h_w	$u_{\tau,\mathrm{cr}}$ (cm/s)
90–100 μm	95 μm	30.0°	16 mm	32.9 ± 0.8
180–200 μm	190 μm	29.0°	15 mm	43.6 ± 0.8
280–300 μm	290 μm	29.5°	16 mm	49.7 ± 0.8
400–425 μm	413 μm	29.5°	19 mm	47.4 ± 0.8

Our experimental setup (see Fig. 1(a)) consists of a 15 mm wide and 58 mm high annular channel of 292 mm diameter formed by a solid inner cylinder and an outer cylinder shell, both made of Perspex. The annular channel is filled with glass beads of density $\rho_\mathrm{s} = 2.45\,\mathrm{g/cm^3}$. The glass beads have been sieved to obtain the size ranges specified in Table 1. The listed values for the angle of repose were measured after having poured the sand slowly into the water-filled channel. The values are close to 30.0°. The depth of the water layer, *i.e.*, the distance between the flat sand surface and the rotor disc at the start of each run, is also given in Table 1.

The channel is lowered into an aquarium that is filled with water to a height of 14 cm. The shear flow is generated with a rotor disc that extends 4 mm from the top into the channel. Since the ripple dynamics is influenced by the initial structure of the sand surface [28], the surface was flattened with a wooden T-shaped plate before each run. Six cameras, controlled by a single frame grabber card, are placed at angular distances of 60° and cover the entire circumference of the channel.

At a constant sampling rate $f_\mathrm{s} = 1/\Delta T_\mathrm{s}$ the images of all six cameras are stored. The boundary between the brighter sand and the darker water is detected, rescaled to account for the geometrical aberration, and the six pieces are matched together. An example is shown in Figure 1(b). The link between two images is indicated by white vertical lines. We detect the sand-water interface with a lateral resolution $\Delta X = \pi \cdot 292\,\mathrm{mm}/2400 \approx 0.38\,\mathrm{mm}$, which is in the range of the particle diameter. The corresponding line is shown in white. The water is flowing from the left to the right.

For quantifying the shear stress exerted by the flowing fluid on the sediment particles two dimensionless parameters have been considered in the literature (see, *e.g.*, Refs. [6,26]): the particle Reynolds number Re_* and the so-called Shields parameter θ. The particle Reynolds number is defined as

$$Re_* = \frac{du_\tau}{\nu},$$

where the relevant length scale is the mean grain diameter d, ν is the kinematic viscosity of water at room temperature, and

$$u_\tau = \left(\nu \frac{\partial U}{\partial y}\right)^{\frac{1}{2}}$$

is the bed shear velocity related to the shear stress acting on the particles. We have estimated $\frac{\partial U}{\partial y}$ by assuming a linear profile for the fluid velocity $U(y)$ in the radial middle of the channel. The Shields parameter is defined as

$$\theta = \frac{u_\tau^2}{g(s-1)d},$$

where $s = (\rho_\mathrm{s} - \rho_\mathrm{f})/\rho_\mathrm{f}$ is the relative density of the sediment, with ρ_s and ρ_f being the density of the sand and of the fluid, respectively, and g is the acceleration due to gravity. In most of this paper we will quantify the applied shear stress through the particle Reynolds number. The corresponding values for the Shields parameter can be obtained from the relation

$$\theta = \frac{Re_*^2 \nu^2}{g(s-1)d^3}.$$

We emphasize that the linear profile assumed for the fluid velocity is merely a convenient way to obtain a characteristic shear stress directly from the set rotation rate of the disc. All values for the particle Reynolds number and the Shields parameter given below rest on this assumption. Had the fluid velocity been determined experimentally in detail over the entire channel, it would have been possible to give more accurate values. The "true" shear velocity is lower than the one obtained from our procedure. This is at least in part caused by the sidewalls in the narrow channel. The flow pattern in the channel is probably turbulent. However, in the immediate vicinity of the bottom where the bed-load movement occurs, one has a laminar boundary layer [29].

As a result of the cylindrical geometry one expects a weak flow component in radial direction. We assume that it does not contribute much to the shear stress.

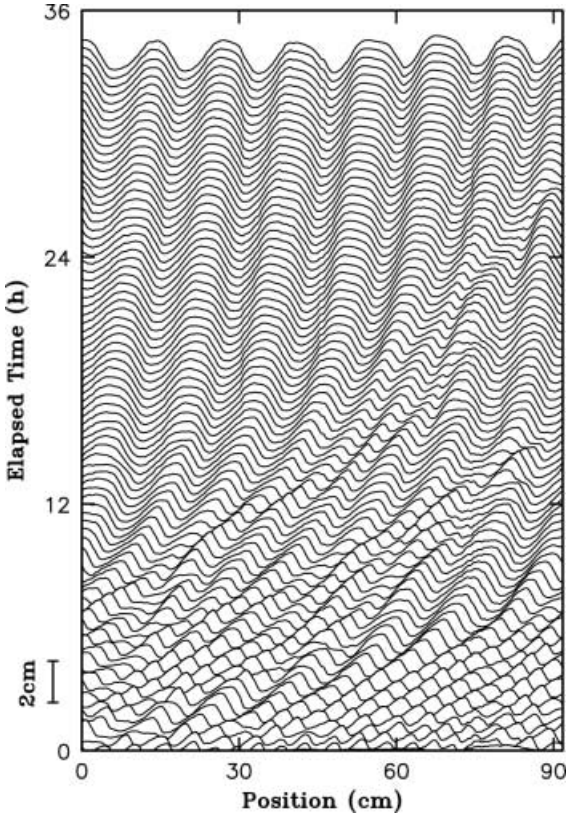

Fig. 2. Spatiotemporal evolution of the sand-water interface along the circumference of the channel. Consecutive data sets are separated 25 min in time and are plotted above each other with a certain offset. The scale is given at the left side of the figure. The grain diameter is $d = 95\,\mu$m.

3 Experimental results

3.1 Ripple evolution

We will first give a qualitative description of the different dynamical stages observed. Figure 2 shows the characteristic behavior of the ripple pattern as a function of time. In this experiment the shear stress was $Re_* = 0.71$ and the sampling time $\Delta T_\mathrm{s} = 25$ min. Between two consecutive boundary curves an offset of 1 mm is added.

In the initial transient regime one observes a state where ripples of quite different dimensions coexist, and where ripples grow, diminish, and merge. This agitated dynamics eventually leads to a stationary state. Figure 3

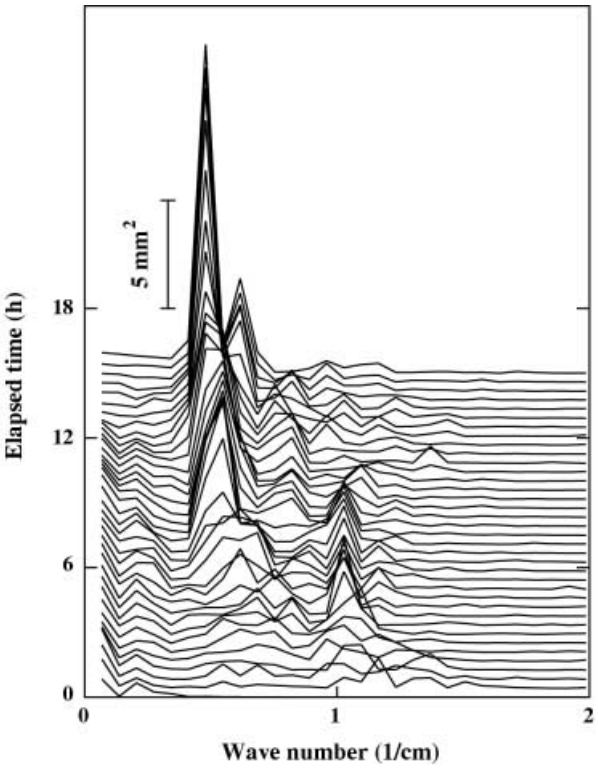

Fig. 3. Spatiotemporal evolution of the first 30 modes of the Fourier series corresponding to the sand-water interface shown in Figure 2. Consecutive data sets are separated 25 min in time and are plotted above each other with a certain offset. The grain diameter is $d = 95\,\mu$m.

shows the "calming down" of the dynamics in Fourier space. After about 15 hours a single mode begins to dominate the spectrum, and the ripples are of approximately the same size. In this state the ripples drift slowly in the downstream direction without significant changes in the mean ripple amplitude. The same behavior is found also for other sand charges with larger grain sizes (see Figs. 4 and 5).

In order to allow for quantitative characterization, the boundary curve $h(x, n\Delta T_\mathrm{s})$, where x is the spatial position and $n\Delta T_\mathrm{s}$ with $n \in N$ the elapsed time, is Fourier decomposed,

$$h(x, n\Delta T_\mathrm{s}) = \frac{a_0}{2} + \sum_{i=1}^{N} \left\{ a_i(n\Delta T_\mathrm{s}) \cos\left(\frac{i2\pi x}{L}\right) + b_i(n\Delta T_\mathrm{s}) \sin\left(\frac{i2\pi x}{L}\right) \right\}, \quad (1)$$

where L is the circumference of the channel and $2N = 2400$ the number of data points in the boundary curve. Four quantities extracted from the data will be of particular importance in what follows: the mean ripple amplitude, the mean sediment transport rate, the mean drift velocity of the ripples, and the mean wave number. Note that all these quantities, as defined below, imply averaging over the circumference of the channel.

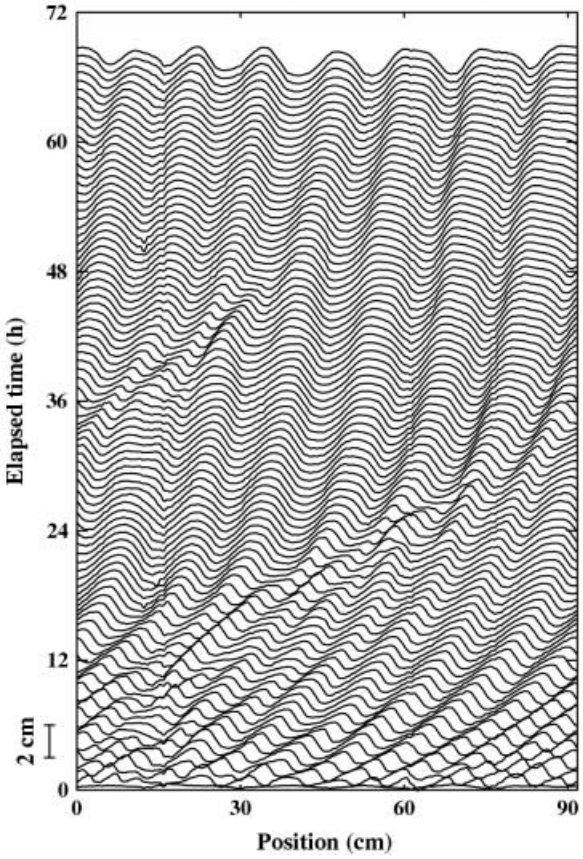

Fig. 4. Spatiotemporal evolution of the sand-water interface along the circumference of the channel. Consecutive data sets are separated 25 min in time and are plotted above each other with a certain offset. The scale is given at the left side of the figure. The grain diameter is $d = 190\,\mu$m.

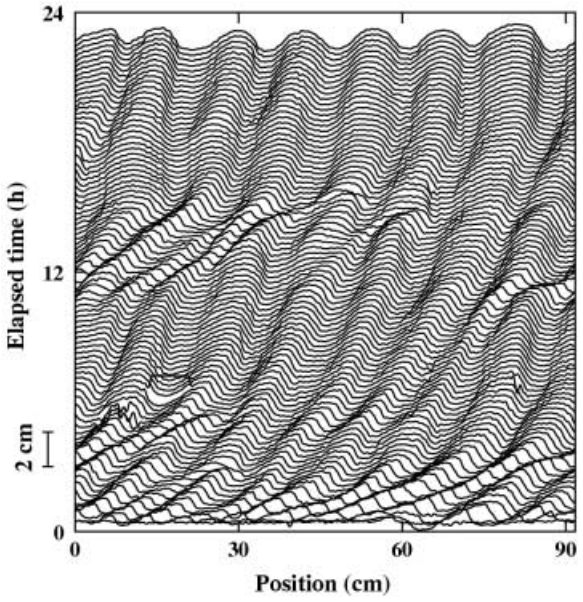

Fig. 5. Spatiotemporal evolution of the sand-water interface along the circumference of the channel. Consecutive data sets are separated 25 min in time and are plotted above each other with a certain offset. The scale is given at the left side of the figure. The grain diameter is $d = 413\,\mu$m.

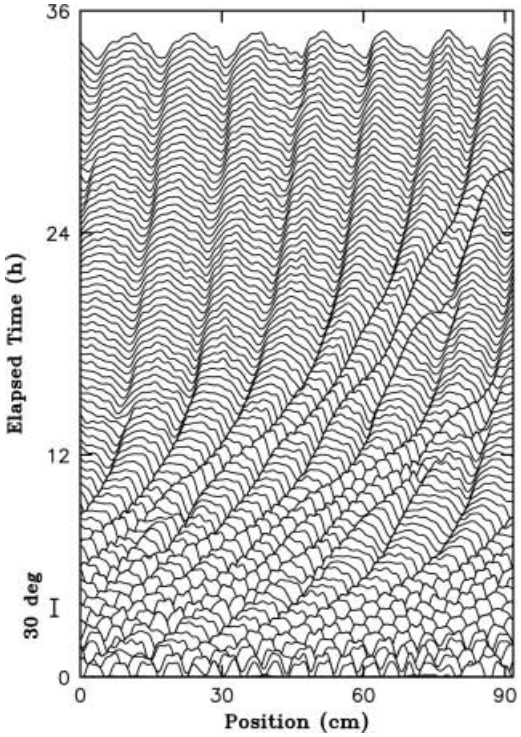

Fig. 6. Spatiotemporal evolution of the local slope $\arctan(\frac{\partial h}{\partial x})$ along the circumference of the channel. Consecutive data sets are separated 25 min in time and are plotted above each other with a certain offset. The scale is given at the left side of the figure. The grain diameter is $d = 95\,\mu$m.

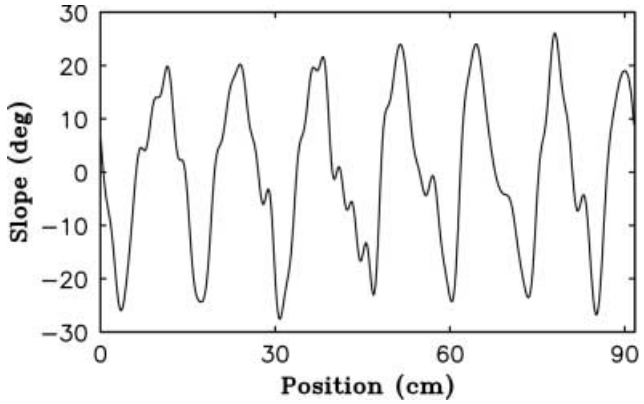

Fig. 7. Local slope $\arctan(\frac{\partial h}{\partial x})$ for the stationary state reached after 30 hours. The grain diameter is $d = 95\,\mu$m.

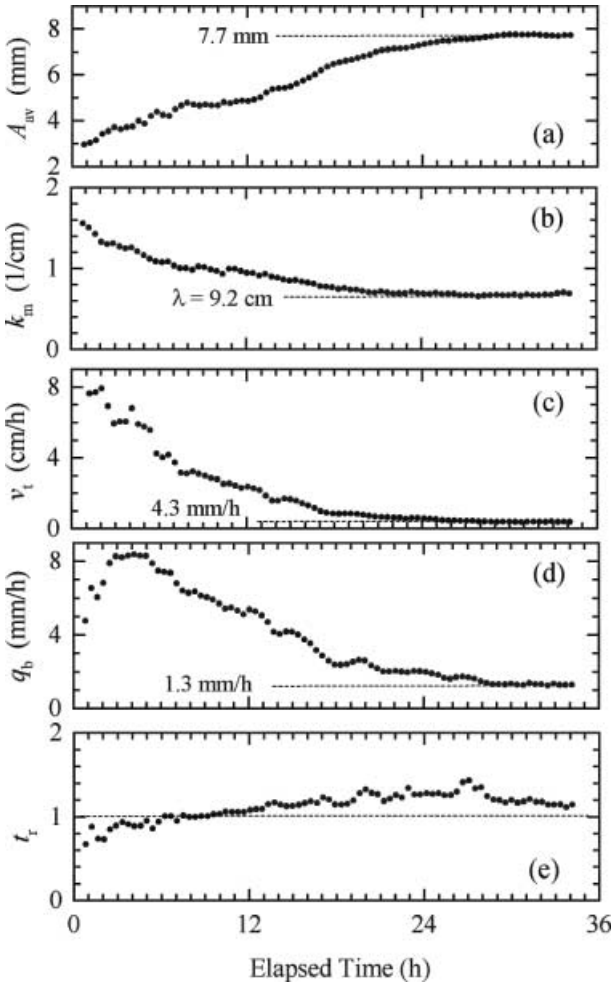

Fig. 8. Temporal evolution of the sediment transport for grains with diameter $d = 95\,\mu$m. The solid circles indicate the measured values for (a) the average amplitude, (b) the wave number, (c) the velocity of the pattern, and (d) the mean transport rate. The dashed lines indicate the steady-state value reached after about 30 hours. In (e) the transport ratio is shown by solid circles, and the dashed line indicates the theoretically expected number, $t_r = 1$.

It is interesting to compare the slope of the evolving ripples with the angle of repose. To do so, we differentiate the boundary curve $h(x)$ using 40 Fourier coefficients and plot the temporal evolution of the local surface angle $\alpha(x) = \arctan(\frac{\partial h}{\partial x})$ for the transient regime (Fig. 6) as well as for the stationary state (Fig. 7).

The ripple amplitude is smaller than the ripple wavelength. The measured slopes remain below the static angle of repose $\alpha = 30.0°$ (see Tab. 1) during all stages of the ripple formation process. One might conclude that spontaneous avalanches in the sand do not play any role in the ripple dynamics. However, one expects the dynamical angle of repose to be lower than the static angle. In fact, the measured local slopes are not far from the static angle of repose at the steepest point on the lee side of the ripple. On the other hand, our data indicate that in the stationary state avalanches cannot be large. This might be different in the earlier stages of the evolution.

The mean ripple amplitude $A_{\rm av}$ of the pattern is given from the Fourier amplitudes as

$$A_{\rm av} = \sqrt{\sum_{i=1}^{N}(a_i^2 + b_i^2)}. \qquad (2)$$

Typical results are presented in Figure 8(a). The mean amplitude $A_{\rm av}$ grows almost linearly for about 24 hours and reaches a maximum value after about 30 h. The

asymptotic value of the ripple amplitude is less than 1 cm, as indicated by the dashed line.

In order to characterize the longitudinal scale of the pattern by a single number, we calculate a mean wave number $k_{\rm m}$, defined as

$$k_{\rm m} = \sqrt{\frac{\sum_{i=1}^{N}(a_i^2+b_i^2)k_i^2}{\sum_{i=1}^{N}(a_i^2+b_i^2)}} \tag{3}$$

with $k_i = \frac{2\pi}{L/i}$. This special choice is motivated by the calculation of the transport ratio presented below. The mean wave number, as indicated in Figure 8(b), decreases monotonically as a result of the merging of ripples in the transient state. Note that the steady-state value for $k_{\rm m}$ does not seem to fit with the number of ripples, because the surface cannot be described by a simple sine wave.

The mean velocity $v_{\rm t}$ of the pattern is obtained by cross-correlating consecutive lines. We compute

$$S(\delta x,t) = \sum_{j=1}^{2N}(h(x_j,t) - h(x_j+\delta x, t+\Delta T_{\rm s}))^2 \tag{4}$$

for a number of values for the spatial trial shift δx. The condition

$$\frac{\partial S(\delta x_{\rm d},t)}{\partial \delta x} = 0 \tag{5}$$

defines the actual shift $\delta x_{\rm d}$ between the two patterns that are being compared. The value is obtained from linear interpolation between discrete values of the difference $S(\delta x+\Delta x,t) - S(\delta x,t)$. Here, Δx denotes the spatial distance between measurement points, see above. The drift velocity of the ripples is then given by

$$v_{\rm t} = \delta x_{\rm d}/\Delta T_{\rm s}\,. \tag{6}$$

The measurements presented in Figure 8(c) clearly indicate that the ripples move fast in the beginning, and slow down to a finite value of about 4.3 mm/h after a transient time of 30 h. A complete revolution of the pattern would then take about 9 days. The observation that for a given grain size the translation speed of the ripples decreases with increasing ripple height was also reported in reference [30].

The measured drift velocity must in some way reflect the typical grain velocity. These two velocities could only be equal had there been stiff translation of the entire ripple. Since only grains in a shallow layer along the sand surface move, the grain velocity must be correspondingly much higher than the drift velocity of the ripples. It is not possible to deduce the depth of the fluidized layer from our data. Let us assume that it is one layer deep. The number of moving grains along one ripple is then proportional to λ/d, while the total number of grains in this region (down to the depth of the ripple trough) is proportional to $A_{\rm av}\lambda/d^2$, where λ is the wavelength of the ripple pattern. Therefore, the number of moving grains divided by the total number of grains is $d/A_{\rm av}$. We obtain an estimate for the mean grain velocity by dividing the drift velocity of the ripples by that ratio. We find a value of about 0.1 mm/s, *i.e.*, 10^{-4} of the speed of the rotor disc.

To obtain a quantitative measure for the sand flux along the surface we use the mean rate of sedimentation and erosion. Due to the transport of sand the local height of the surface varies slowly. We measure the sediment transport rate as

$$q_{\rm b} = \sqrt{\langle(\Delta h\ /\Delta T_{\rm s})^2\rangle_{\rm s}}\,, \tag{7}$$

where $\langle ...\rangle_{\rm s}$ denotes the spatial average, and $\Delta T_{\rm s}$ is the sampling time of 25 minutes. The measurements presented in Figure 8(d) indicate an increasing transport rate in the beginning of the experiment followed by a monotonic decrease. The initial increase is caused by radial rearrangement of the sand, and the final decrease is due to the slowing down of the ripples.

We now turn to a quantitative analysis of the coupling between ripple amplitude, drift velocity, and sediment transport rate. From mass conservation we expect $q_{\rm b}$, $v_{\rm t}$, $A_{\rm av}$, and $k_{\rm m}$ to be related, as suggested in references [21,22]. However, for the interpretation of the experimental data one has to take into consideration the finite sampling time. Our starting point is the equation of continuity,

$$\frac{\partial \rho}{\partial t} + \nabla(\rho \mathbf{v}) = 0\,. \tag{8}$$

Here, ρ is the density of the sediment, and $\mathbf{v}$ its velocity. Experimentally, we only determine the height h of the sand at the outer channel wall, and calculate from it a velocity component v along the wall. Thus, we cannot measure any motion of sand grains in radial direction. We assume that the grains basically follow concentrical tracks in the channel, so that the dynamical behavior at the outer wall is fully representative. This assumption will be more precisely discussed now.

With $\rho = h\phi$ and a constant value for the packing fraction ϕ we obtain an equation of continuity for the motion of sand along the outer channel wall as

$$\frac{\partial h}{\partial t} + h\frac{\partial v}{\partial x} + v\frac{\partial h}{\partial x} = 0\,. \tag{9}$$

Under stationary conditions we expect the velocity v to be constant, thus

$$\frac{\partial h}{\partial t} = -v\frac{\partial h}{\partial x}\,. \tag{10}$$

The sediment transport rate,

$$Q_{\rm b} \equiv \sqrt{\left\langle\left(\frac{\partial h}{\partial t}\right)^2\right\rangle_{\rm s}}\,, \tag{11}$$

may be expressed as

$$Q_{\rm b}^2 = v^2\left\langle\left(\frac{\partial h}{\partial x}\right)^2\right\rangle_{\rm s}\,. \tag{12}$$

The mean spatial derivative can be expressed in terms of Fourier coefficients,

$$Q_{\rm b}^2 = v^2\sum_{i=1}^{N} k_i^2(a_i^2/2 + b_i^2/2)\,, \tag{13}$$

and using equation (3) we obtain

$$Q_{\rm b}^2 = v^2 k_{\rm m}^2 \sum_{i=1}^{N} (a_i^2/2 + b_i^2/2)\,. \tag{14}$$

Therefore, the sediment transport rate may be written as

$$Q_{\rm b} = v k_{\rm m} A_{\rm av}/\sqrt{2}\,. \tag{15}$$

The measured transport rate $q_{\rm b}$ is smaller than the true rate $Q_{\rm b}$ due to the finite sampling time Δt: harmonic waves $h(x,t) = \sin(kx + \omega t)$ are measured with a frequency-dependent reduction factor α given by

$$\alpha^2 = \frac{\left\langle \left(\frac{\Delta h}{\Delta t}\right)^2 \right\rangle_{\rm s}}{\left\langle \left(\frac{{\rm d}h}{{\rm d}t}\right)^2 \right\rangle_{\rm s}}\,. \tag{16}$$

Therefore,

$$\alpha^2 = \frac{\left\langle \left(\frac{\sin(kx+\omega(t+\Delta t))-\sin(kx+\omega t)}{\Delta t}\right)^2 \right\rangle_{\rm s}}{\langle(\omega\cos(kx+\omega t))^2\rangle_{\rm s}} \tag{17}$$

and we find

$$\alpha^2 = \left(\frac{\sin(\frac{\omega\Delta t}{2})}{\frac{\omega\Delta t}{2}}\right)^2\,. \tag{18}$$

The factor α gives the reduction of the measured transport rate $q_{\rm b}$ as compared to the true rate $Q_{\rm b}$, $q_{\rm b} = \alpha Q_{\rm b}$. Thus, in equation (15) we have to scale down the rms value accordingly before we make a comparison. Since the reduction factor depends on frequency, this involves both $k_{\rm m}$ and $A_{\rm m}$ (see Eqs. (2) and (3)). Thus, our measured $q_{\rm b}$ corresponds to an effective amplitude

$$A_{\rm eff} = \sum_{i=1}^{N} (a_i^2 + b_i^2)\alpha_i^2\,, \tag{19}$$

where $\alpha_i^2 = (\frac{\sin(\phi_{\rm s})}{\phi_{\rm s}})^2$ is the damping coefficient for wave number k_i, with $\phi_{\rm s} = v_{\rm t}\Delta T_{\rm s} k_i/2$. Similarly, an effective wave number is given by

$$k_{\rm eff} = \sqrt{\frac{\sum_{i=1}^{N}(a_i^2+b_i^2)k_i^2\alpha_i^2}{\sum_{i=1}^{N}(a_i^2+b_i^2)\alpha_i}}\,. \tag{20}$$

To check to which extent the experimental data fit equation (15) we calculate the transport ratio

$$t_{\rm r} = q_{\rm b}/(v_{\rm t} k_{\rm eff} A_{\rm eff}/\sqrt{2})\,. \tag{21}$$

We expect $t_{\rm r} = 1$ under the conditions discussed above. The experimental results are shown in Figure 8(e). The deviations from 1 are always less than 30%, and after a transient of about 30 hours the value 1 seems to be reached fairly precisely, indicating that the ripples now move as a stationary pattern without considerable change of packing density and without considerable radial transport of the sand. This is consistent with Figure 2.

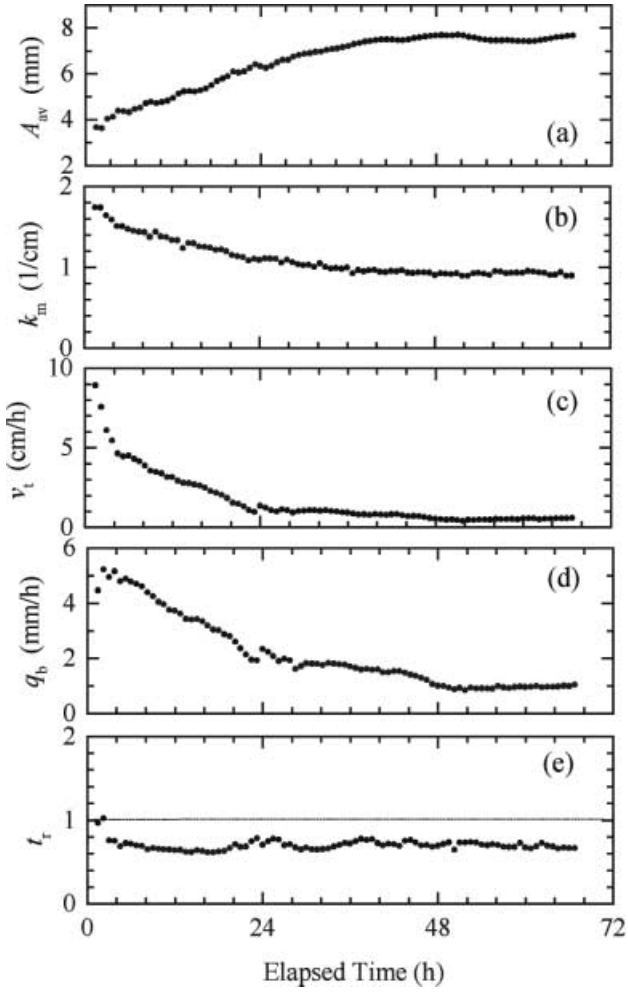

Fig. 9. Temporal evolution of the sediment transport for grains with diameter $d = 190\,\mu$m. The solid circles indicate the measured values for (a) the average amplitude, (b) the wave number, (c) the velocity of the pattern, and (d) the mean transport rate. In (e) the transport ratio is shown by solid circles, and the straight line indicates the theoretically expected number, $t_{\rm r} = 1$.

However, it is remarkable that $t_{\rm r}$ is quite close to 1 also during the early stages in the ripple dynamics. As shown in parts (a)-(d) of Figure 8, all the quantities that enter $t_{\rm r}$ change much more during the experiment. In this sense $t_{\rm r}$ is a useful quantitative characterization of the coupling between ripple size and sediment transport rate: during all stages in the dynamical evolution the effects balance to have $t_{\rm r} \simeq 1$. The steady state is then reached after a fine tuning of this balance. We find the same behavior also for other sand charges with larger grain sizes (see Figs. 9 and 10).

A close relation between the transport rate and the evolution of the sand-water interface can be found also locally: the deviations from $t_{\rm r} = 1$ are smallest in those parts of the channels where the ripples are closest to steady-state shape. If equation (10) holds locally, the expression

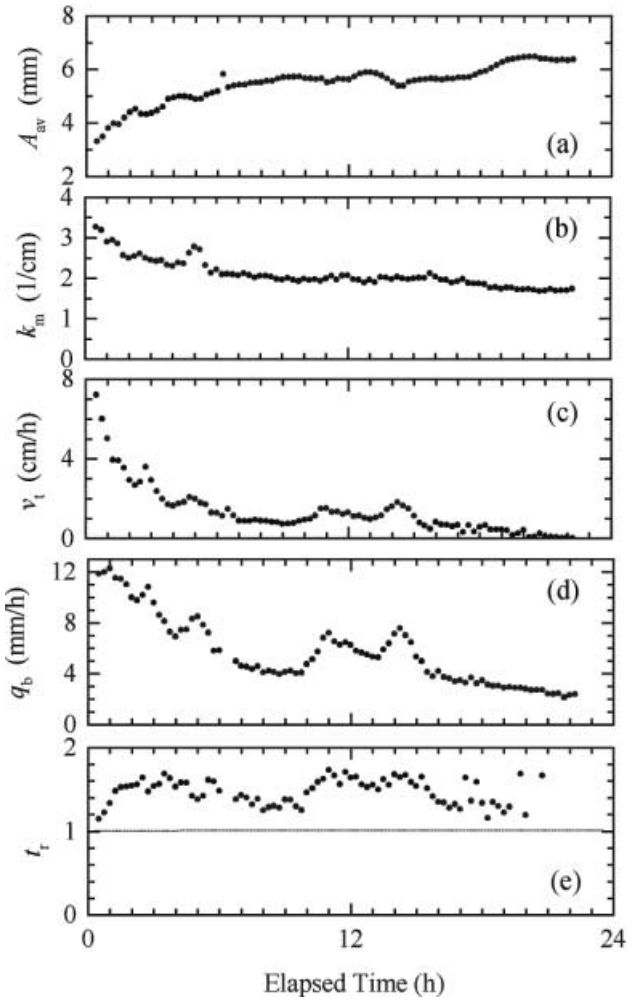

Fig. 10. Temporal evolution of the sediment transport for grains with diameter $d = 413\,\mu$m. The solid circles indicate the measured values for (a) the average amplitude, (b) the wave number, (c) the velocity of the pattern, and (d) the mean transport rate. In (e) the transport ratio is shown by solid circles, and the straight line indicates the theoretically expected number, $t_r = 1$.

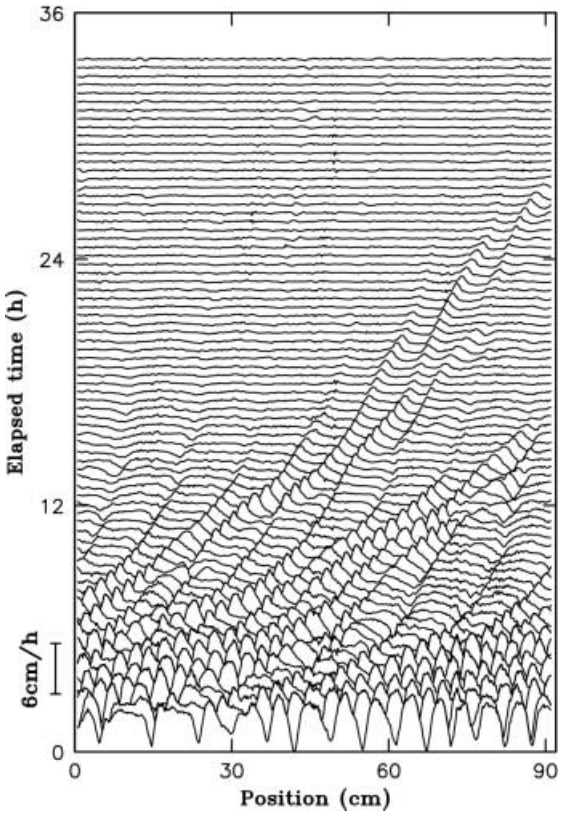

Fig. 11. Spatiotemporal evolution of $\frac{\partial h}{\partial t} + v\frac{\partial h}{\partial x}$ along the circumference of the channel. Consecutive data sets are separated 25 min in time and are plotted above each other with a certain offset. The scale is given at the left side of the figure. The grain diameter is $d = 95\,\mu$m.

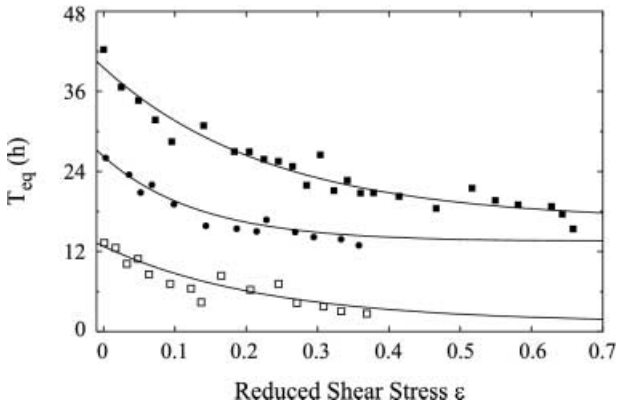

Fig. 12. The time T_{eq} needed to reach the stationary state, as a function of the reduced shear stress excess ϵ, for grain sizes $d = 95\,\mu$m (■), $d = 190\,\mu$m (●) and $d = 413\,\mu$m (□).

$\frac{\partial h}{\partial t} + v\frac{\partial h}{\partial x}$ must be zero. In order to check this condition, the spatial and time derivatives as well as the average velocity v of the whole ripple pattern were determined individually from the measured data. As demonstrated in Figure 11, local deviations from zero can be found in regions where smaller ripples merge to form a larger ripple with the proper size, shape and speed. In these areas the local velocity $v(x)$ is not yet equal to the final average drift velocity v, *i.e.*, the local velocity gradient $\frac{\partial v}{\partial x} \neq 0$, which causes an imbalance to equation (10). After a transient of 30 h all local deviations have vanished and the rippled surface reaches its stationary conformation.

The measurements shown so far clearly indicate that there is a stationary state of the ripples. The time T_{eq} to reach this state is influenced by the grain size and the driving force. This is shown in Figure 12. The driving force as given by the rotation rate is presented in a dimensionless form by $\epsilon = \omega/\omega_{cr} - 1$. ω_{cr} is the critical rotation speed at which ripples are first formed. As ϵ decreases towards the threshold for ripple formation, T_{eq} increases in a monotonic way. The lines are supposed to guide the eye. The upper curve corresponds to the smallest grain size used. It is interesting to note that one deals with the longest waiting times in that case. One could speculate that this is due to a higher mobility of larger particles: smaller grains

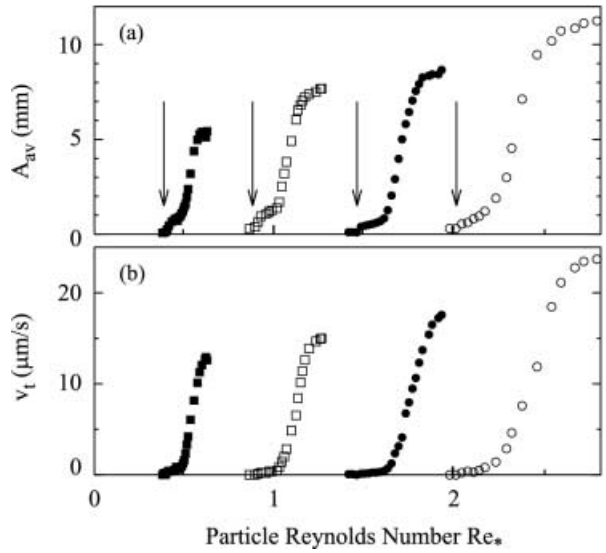

Fig. 13. Dependence of the average amplitude $A_{\rm av}$ (a) and the drift velocity $v_{\rm t}$ (b) on the particle Reynolds number Re_* for grain size $d = 95\,\mu$m (■), $d = 190\,\mu$m (□), $d = 290\,\mu$m (●), and $d = 413\,\mu$m (○). The arrows indicate the onset of ripple formation.

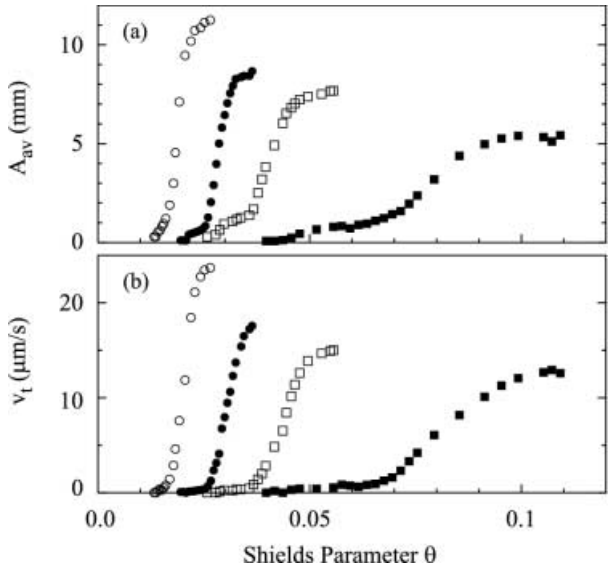

Fig. 14. Dependence of the average amplitude $A_{\rm av}$ (a) and the drift velocity $v_{\rm t}$ (b) on the Shields parameter θ for grain size $d = 95\,\mu$m (■), $d = 190\,\mu$m (□), $d = 290\,\mu$m (●), and $d = 413\,\mu$m (○).

are more easily halted, and thus a larger number of grain shifts and a longer time is needed to reach the steady state.

3.2 Scaling

An important question is whether it is possible to obtain a scale-independent description of the ripple dynamics. How should one rescale data obtained using different grain sizes? Experiments have been carried out using four different mean particle diameters (see Tab. 1). We focus on average quantities in the stationary state, which we expect to give the most robust characterization of the ripple dynamics. We use the two dimensionless parameters Re_* and θ to characterize the driving rate. In what follows, the average value of ripple amplitude or drift velocity refers to the average over temporal fluctuations taken after reaching the stationary state (dashed lines in Fig. 8). Note that, by our definition of these quantities, spatial averaging is always implied.

The dependence of the average amplitude $A_{\rm av}$ and the drift velocity $v_{\rm t}$ on the particle Reynolds number Re_* for four different grain sizes is given in Figure 13. The four curves display a strikingly similar S shape. However, the curves do not collapse when given as functions of Re_*, which is proportional to d. Instead, they are shifted to higher values of Re_* for increasing grain size. Furthermore, the curves are stretched in the vertical direction when the grain diameter increases.

Our observations are consistent with the trends seen in previous experimental studies. The steady-state ripple amplitude seems to increase with the grain diameter [27] for comparable stream conditions, whereas for a given grain size it tends to increase with Re_* [18]. In reference [30] the translation speed of ripples was found to be dependent on the shear stress *via* a power law with a positive exponent, but no dependence on the grain diameter was found. No experimental studies focussing on the scaling of the sediment transport are known to us. An increase in the critical particle Reynolds number $Re_{*\rm cr}$ with increasing mean diameter was also observed in reference [25]. However, a quantitative comparison between those and our experiments is not feasible, since the sand used in the experiments of Mantz [25] was flaky.

In Figure 14 the dependence of the average amplitude $A_{\rm av}$ and the drift velocity $v_{\rm t}$ on the Shields parameter θ for the four different grain sizes is given. The similarity in the shape of the curves and their stretching in the vertical direction mentioned above can be observed also here. Note that the curves appear in reverse order, since $\theta \propto d^{-1}$. Previous studies have found the onset of grain motion to occur for Shields parameter values of 0.04 and higher, while we find in our experiments that ripples are formed at lower values, in particular for large grain sizes.

We point out that our results shown in Figures 13 and 14 indicate that neither the particle Reynolds number nor the Shields parameter capture correctly the onset of ripple formation. In terms of these dimensionless numbers the onset value does not coincide, but is systematically shifted as the grain size is varied. Thus, neither the particle Reynolds number nor the Shields parameter can serve as basis for a scale-free description of the onset of ripple formation, since they do not contain the correct size dependence.

We will now demonstrate that another quantity that does not contain d at all, the bed shear stress, has a value at threshold that is close to constant over the different grain sizes we have investigated.

The values we have obtained for the critical bed shear velocity $u_{\tau,\rm cr}$ are listed in Table 1. The dependence of the

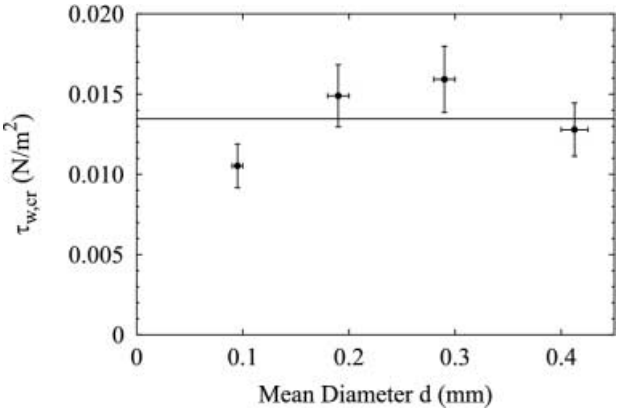

Fig. 15. Dependence of the critical bed shear stress $\tau_{\mathrm{w,cr}}$ on the mean grain diameter d. The straight line indicates the mean value of the four data points.

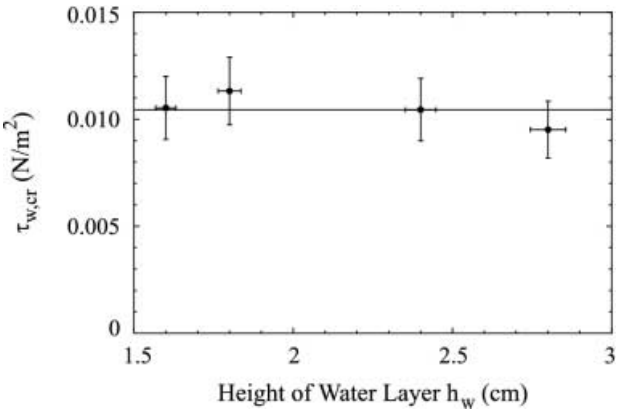

Fig. 16. Dependence of the critical bed shear stress $\tau_{\mathrm{w,cr}}$ on the height of the water layer h_{w} for $d = 95\,\mu$m. The straight line indicates the mean value of the four data points.

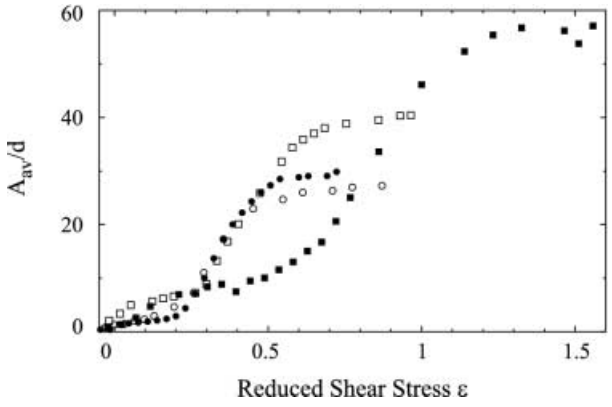

Fig. 17. Dependence of the rescaled average amplitude A_{av}/d on the reduced shear stress excess ϵ for grain size $d = 95\,\mu$m (■), $d = 190\,\mu$m (□), $d = 290\,\mu$m (●), and $d = 413\,\mu$m (○).

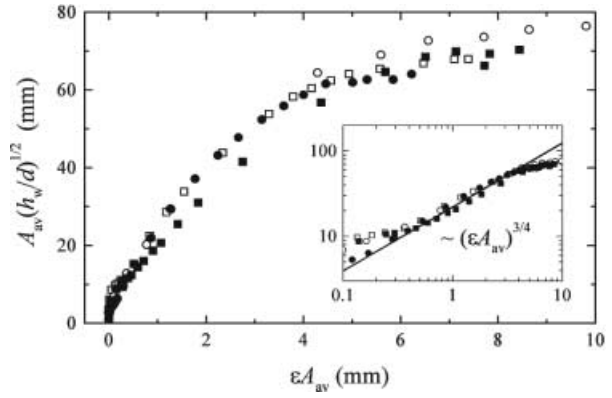

Fig. 18. Rescaled average amplitude $A_{\mathrm{av}}(\frac{h_{\mathrm{w}}}{d})^{\frac{1}{2}}$ as a function of ϵA_{av} for grain size $d = 95\,\mu$m (■), $d = 190\,\mu$m (□), $d = 290\,\mu$m (●), and $d = 413\,\mu$m (○). The inset shows the same data with logarithmic scales.

critical bed shear stress $\tau_{\mathrm{w,cr}} = \rho_{\mathrm{f}} u^2_{\tau,\mathrm{cr}}$ on the mean grain diameter is given in Figure 15. The error bars in the horizontal direction reflect the widths of the grain size distributions as given in Table 1. The vertical error bars give the uncertainty of the determination of the critical bed shear velocity. The average over the data is indicated by the line in Figure 15. To a first approximation the critical bed shear stress does not depend on the grain size. Nevertheless, this statement is based on four data points only, and therefore any conclusions should be drawn with caution.

We have also checked for a possible influence from the depth (height) of the water layer on the threshold value. In Figure 16 the dependence of the critical bed shear stress $\tau_{\mathrm{w,cr}}$ on the height of the water layer for a fixed grain size of $d = 95\,\mu$m is shown. The average over the data is given by the straight line. The error bars reflect the experimental uncertainties in determining the critical bed shear stress and the height of the water layer, respectively. One must conclude that the water height has no influence on the threshold value of the bed shear stress.

Returning now to the full curves in Figure 13, the evolution in the curve shapes with increasing grain size is so regular that one expects some kind of data collapse to be possible. An apparently plausible choice is to measure the ripple amplitude in grain sizes and quantifying the driving in terms of the bed shear stress discussed above. In Figure 17 the rescaled amplitude A_{av}/d is given as a function of the reduced shear stress excess $\epsilon = (\tau_{\mathrm{w}} - \tau_{\mathrm{w,cr}})/\tau_{\mathrm{w,cr}}$. Apparently, the assumed scaling law $A/d = f(\epsilon)$ does not describe the data satisfactorily. Neither the level of the steady-state plateau (as was also observed above), nor the first crossover from a lower to a higher slope in the curves, nor the second crossover where the slope decreases again towards the steady-state plateau coincides. This indicates that there is no unique scaling of the amplitude in terms of the grain size that is also independent of the shear stress excess ϵ.

We have explored several additional rescalings of the data. The most promising of these is shown in Figure 18 where $A_{\mathrm{av}}(\frac{h_{\mathrm{w}}}{d})^{\frac{1}{2}}$ is given as a function of ϵA_{av}. The data can be fitted with a power law $\sim (\epsilon A_{\mathrm{av}})^{3/4}$. From this, a relation between A_{av} and ϵ can be deduced as

$$A_{\mathrm{av}} \sim \left(\frac{d}{h_{\mathrm{w}}}\right)^2 \cdot \epsilon^3. \tag{22}$$

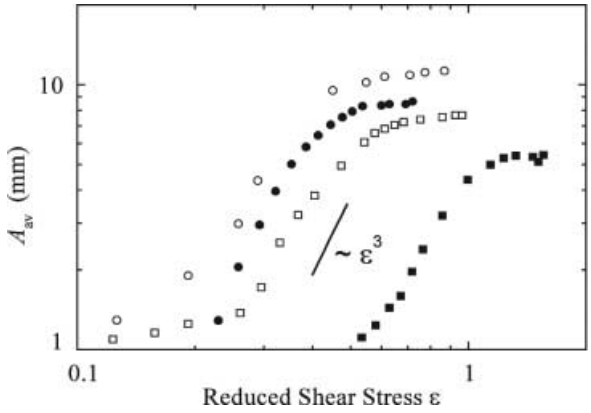

Fig. 19. Dependence of the average amplitude $A_{\rm av}$ on the reduced shear stress excess ϵ for grain size $d = 95\,\mu$m (■), $d = 190\,\mu$m (□), $d = 290\,\mu$m (●), and $d = 413\,\mu$m (○). The straight line indicates a power law $A_{\rm av} \sim \epsilon^3$.

This is illustrated in Figure 19. An ϵ^3-dependence of the sand flux is well known from Bagnold's pioneering work [1]. Here we have found a similar relationship for the ripple amplitude, at least in an intermediate range of the driving shear stress. For higher ϵ-values, however, this cubic dependence is replaced by a saturation of the ripple amplitude.

4 Summary and conclusion

We have found in our experiments that the quantities ripple amplitude, drift velocity and sediment transport rate are coupled. This is explained on the basis of a continuity equation for the sand. The dynamics is governed by a feedback mechanism between ripple amplitude and sediment transport rate. This feedback can be quantitatively expressed in terms of a transport ratio, which is close to constant during the entire experiment. Thus, even though the amplitude, velocity, and sediment transport all change significantly during an experiment, the balance between them is not much altered.

In our experimental setup the ripple pattern reaches a stationary state characterized by a very slow drift, finite amplitude and wavelength. The time needed to reach that state can be fairly long, however.

Neither the particle Reynolds number nor the Shields parameter capture the onset correctly. In fact, we could not find any influence of the particle diameter or the water height. Instead, the onset of ripple formation seems to depend on the shear stress alone.

Universal laws for the scaling of the amplitude, the drift velocity and the sediment transport rate independent of the shear stress could not be found. However, there are indications of a relationship of the form $A_{\rm av} \sim \epsilon^3$. To pursue this point experimentally a larger setup, which would allow the average ripple amplitude to reach higher values before saturation, would be necessary.

Due to the channel geometry only an integer number of ripples is possible. Thus, our apparatus may have changed the ripple wavelength that is observed as compared to the one in a very large system. In view of the coupling between the ripple dimensions and the sediment transport that drives the dynamics, this imposed wavelength may well have influenced the ripple amplitude in the steady state.

It remains an open question how important the finite-size effect is. One could speculate that with increasing system size significant changes may occur in the ripple dynamics as one passes from one dominating box mode to another. Following this logic, the dynamics for fixed system size may be frustrated between two box modes. On the other hand, in nature one hardly encounters closed systems like our experimental setup. Consequently, ripples are expected to evolve without any coupling to externally imposed box modes. Therefore, both the ripple shape and the existence and characteristics of a stationary state may very will be quite different in our experiments as compared to nature. This issue can only be resolved through further experimental studies.

Another important limitation of the setup is the fact that our channel is fairly shallow. In addition, the rotor disc provides rigid boundary conditions for the water flow on the upper surface. This might have a large influence on the final size of the ripples, but presumably does not influence their onset very much, where the amplitude is small compared to the height of the water layer.

An important direction for future research is to correlate the detailed shape of a ripple to its growth, decay, and drift velocity. From such investigations one would hope to learn more on the physical mechanisms of the ripple dynamics.

Another challenge for future experimental work is to enlarge the system in order to reduce finite-size effects. However, this will induce additional difficulties: increasing the channel height will increase the Reynolds number associated with the critical rotation speed, *i.e.*, the turbulence level would increase. Moreover, an increased channel width may alter the radial flow. To overcome that difficulty one would then need to increase the diameter of the whole apparatus, which might lead to a prohibitive long transient time, if one assumes that the period for one ripple revolution around the channel (which is about 9 days in our experiment) is a significant time scale here. Finally, a larger setup will be more demanding as for mechanical stability, since a larger rotor disc, higher rotation rates, and higher motor power would be necessary.

Other important parameters for the ripple dynamics might be the density difference between sand and fluid, and the viscosity of the driving fluid. We are presently exploring the effects of changes in some of these parameters.

We thank G. Straßburger, A. Breu, and C. Völtz for experimental help and clarifying discussions. We are grateful for support from Deutsche Forschungsgemeinschaft through Re 588/12.

References

1. R.A. Bagnold, *The Physics of Blown Sand and Desert Dunes* (Chapman & Hall, London, 1941).
2. A.J. Raudkivi, Proc. Am. Soc. Civil Eng., J. Hydraulics Div. **89**, 15 (1963).
3. P.B. Williams, P.H. Kemp, Proc. Am. Soc. Civil Eng., J. Hydraulics Div. **97**, 505 (1971).
4. A. Betat, V. Frette, I. Rehberg, Phys. Rev. Lett. **83**, 88 (1999).
5. J.F. Kennedy, Ann. Rev. Fluid Mech. **1**, 147 (1969).
6. F. Engelund, J. Fredsøe, Ann. Rev. Fluid Mech. **14**, 13 (1982).
7. J.F. Kennedy, J. Fluid Mech. **16**, 521 (1963).
8. B.M. Sumer, M. Bakioglu, J. Fluid Mech. **144**, 177 (1984).
9. H. Nakagawa, T. Tsujimoto, J. Hydraulics Eng. **110**, 467 (1984).
10. H.-K. Liu, Proc. Am. Soc. Civil Eng., J. Hydraulics Div. **83**, 1 (1957).
11. F. Charru, H. Mouilleron-Arnould, J. Fluid Mech. **452**, 303 (2002).
12. D. Leighton, A. Acrivos, Chem. Eng. Sci. **41**, 1377 (1986).
13. H. Nishimori, N. Ouchi, Phys. Rev. Lett. **71**, 197 (1993).
14. N.B. Ouchi, H. Nishimori, Phys. Rev. E **52**, 5877 (1995).
15. W. Landry, B.T. Werner, Physica D **77**, 238 (1994).
16. R.G. Jackson, J. Fluid Mech. **77**, 531 (1976).
17. L.M.J. Brush *et al.*, Proc. Am. Soc. Civil Eng., J. Hydraulics Div. **92**, 51 (1966).
18. A. Jopling, D.L. Forbes, Geogr. Ann. **61**, 67 (1979).
19. J.H. Baas, Sedimentology **41**, 185 (1994).
20. F.M. Exner, *Ergebnisse der Kosmischen Physik, I. Band* (Akademie-Verlag, Leipzig, Germany, 1931), Chapt. 3, pp. 373-445.
21. H. Ertel, Monatsber. Deutsch. Akad. Wiss. Berlin **8**, 713 (1965).
22. A. Führböter, Mitt. Franzius-Institut für Grund- und Wasserbau der Techn. Hoch. Hannover, Germany No. 29 (1967).
23. M.S. Yalin, Proc. Am. Soc. Civil Eng., J. Hydraulics Div. **103**, 439 (1977).
24. M.S. Yalin, *Mechanics of Sediment Transport*, 2nd edition (Pergamon Press, London, 1977).
25. P.A. Mantz, Sedimentology **25**, 83 (1978).
26. S.E. Coleman, B.W. Melville, J. Hydraulics Eng. **122**, 301 (1996).
27. A.J. Raudkivi, J. Hydraulics Eng. **123**, 58 (1997).
28. J.B. Southard, J.R. Dingler, Sedimentology **16**, 251 (1971).
29. K. Stelczer, *Bed-load Transport, Theory and Practice*, (Water Resources Publications, Littleton, 1981).
30. J. Kühlborn, Ber. Inst. Wasserbau der Techn. Hoch. Darmstadt, Germany No. 49 (1993).